IEEE Open Journal of
Industry Applications

Received 17 March 2020; revised 6 June 2020 and 13 July 2020; accepted 14 July 2020. Date of publication 23 July 2020;
date of current version 26 August 2020. The review of this article was arranged by Editor E. B. Agamloh.

Digital Object Identifier 10.1109/OJIA.2020.3011395

Source of Acoustic Noise in a 12/16 External-Rotor Switched Reluctance Motor: Stator Tangential Vibration and Rotor Radial Vibration

JIANBIN LIANG, BROCK HOWEY (Member, IEEE), BERKER BILGIN (Senior Member, IEEE), AND ALI EMADI (Fellow, IEEE)

McMaster Automotive Resource Centre (MARC), McMaster University, Hamilton, ON L8P 0A6, Canada

CORRESPONDING AUTHOR: JIANBIN LIANG (e-mail: liangj31@mcmaster.ca).

This work was supported in part by the Canada Excellence Research Chairs (CERC) Program, and in part by Natural Sciences and Engineering Research Council of Canada (NSERC).

ABSTRACT Compared with internal-rotor switched reluctance motors (SRMs), external-rotor (ER) SRMs can show different vibration and acoustic noise behavior due to the differences in the designs, e.g. thinner rotor back iron to achieve smaller inertia, and longer stator pole height to improve the electromagnetic performance. This paper presents the considerations in the modeling and analysis of the acoustic noise sources of an ER SRM stator and rotor. The harmonic components of the stator tangential force density and rotor radial force density are analyzed and compared. The vibration modes, the vibration behavior, and acoustic noise of the stator and rotor are also compared. A 12/16 external-rotor SRM designed for a direct-drive E-bike application is used for the modeling, analysis, and experimental validation of vibration and acoustic noise. It is concluded that both the stator tangential vibration and the rotor radial vibration can be sources of the acoustic noise in an ER SRM.

INDEX TERMS Acoustic noise, external-rotor SRM, source.

I. INTRODUCTION

Low acoustic noise is often desired in the design of external-rotor motors for acoustic-noise-sensitive applications, e.g. E-bike applications. Recent studies on the modeling and analysis of the acoustic noise in permanent magnet synchronous external-rotor (ER) motors have been presented in [1]–[4]. Due to the robust structure and low cost, the ER switched reluctance motor is an attractive alternative to the permanent magnet motor. However, a limited number of studies have been conducted for the modeling and analysis of the acoustic noise in ER SRMs [5]. It has also not been studied in detail in the literature whether the tangential vibration in the stator of ER SRM can contribute to the total acoustic noise.

In internal-rotor (IR) SRMs, the radial vibration of the stator back iron is often the primary source of the acoustic noise [6]–[10]. Due to the solid rotor structure of the internal-rotor SRMs, the acoustic noise caused by the vibration of the rotor is often negligible. The stator and rotor pole heights are often short enough in IR SRMs so that the natural frequencies of the tangential modes of the poles are usually high. Thus, the acoustic noise caused by the tangential vibration of the stator and rotor poles is often negligible.

However, this is not necessarily the case for the ER SRMs. Due to the differences in the designs compared with the IR SRMs, ER SRMs can show different vibration and acoustic noise behavior in the stator and the rotor. For example, the rotor back-iron of the ER SRM is often designed with a small thickness in order to reduce the inertia, and the stator can sometimes be designed with a long pole height to increase coil strands and reduce copper loss [11]–[13]. These design differences make the acoustic noise modeling and analysis of the ER SRMs different from the IR SRMs. The thin rotor back iron affects the modal stiffness and the mass of the rotor-endcaps subassembly. This further impacts the

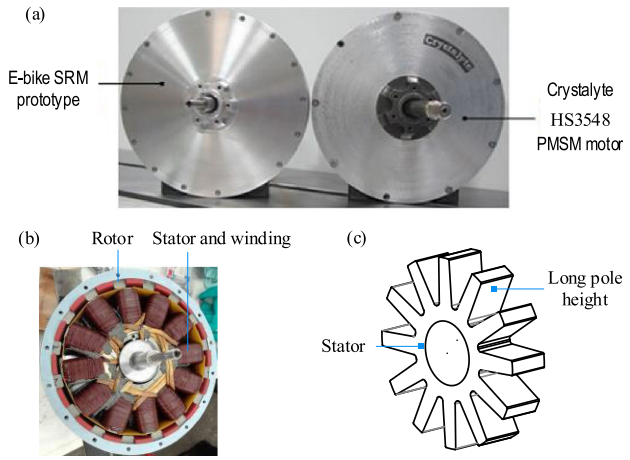

FIGURE 1. 12/16 external-rotor SRM prototype: (a) SRM prototype and the commercial Crystalyte HS3548 PMSM motor, (b) interior of the SRM prototype, (c) CAD drawing of the stator [14].

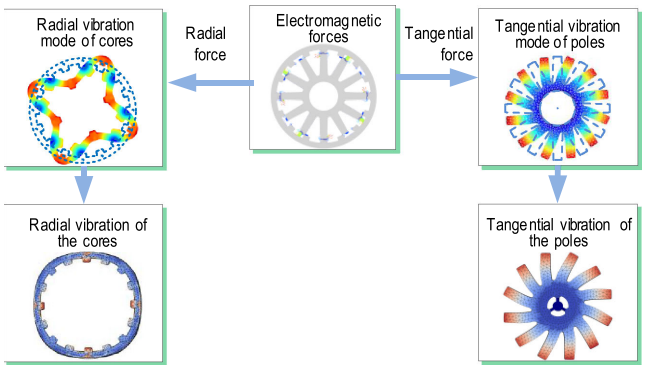

FIGURE 2. Tangential and radial vibration in SRMs.

natural frequencies of the dominant radial vibration modes of the rotor-endcaps subassembly. Besides, if a long stator pole height is adopted in the design of an ER SRM, it tends to decrease the stiffness in the tangential direction and, thus, reduce the natural frequencies of the tangential vibration modes. All the aforementioned features of the ER SRMs can make the tangential vibration of the stator poles one of the sources of acoustic noise in ER SRMs.

This paper aims to model and analyze the vibration behavior and the acoustic noise in ER SRMs. One issue that this paper intends to address is whether the radial vibration of the rotor back iron or the tangential vibration of the stator poles is the primary source of the acoustic noise in ER SRMs. First, two numerical models will be built to simulate the vibration and acoustic noise in the rotor-endcaps and the stator-shaft subassemblies, respectively. Then, the vibration modes, the electromagnetic force density harmonics, the vibration and acoustic noise behavior of the stator and the rotor will be compared. A 12/16 ER SRM designed for a direct-drive E-bike application will be used for the modeling and analysis of vibration and acoustic noise in this paper.

II. DESIGN OF 12/16 EXTERNAL-ROTOR SRM FOR E-BIKE TRACTION APPLICATION

The 12/16 ER SRM is designed based on the geometry constraints and performance targets of the commercial Crystalyte HS3548 E-bike motor (see Fig. 1), which is a surface permanent magnet synchronous motor [12]–[15]. The axial length, stack length, and the outer diameter of the motor are 52.5 mm, 39.5 mm, and 220 mm, respectively. The motor can operate at its max speed, 400 RPM, with 36 V DC link voltage. The rated power of the 12/16 ER SRM is 0.91 kW and the motor was designed with a peak phase reference current of 75A that achieves the same RMS phase current as the commercial PMSM motor. In [12], different pole configurations have been compared and evaluated, and it was concluded that a 12/16 SRM can provide the best performance in terms of average torque, torque quality, and efficiency. Fig. 1 shows the geometry and the prototype of the 12/16 ER SRM. It can be observed that the pole height of the stator is much larger than that of the rotor, and the rotor back iron is thin. This paper will discuss how these design features affect the vibration behavior and acoustic noise in ER SRMs. It should be noted that the acoustic noise modeling and analysis presented in this paper is limited to the airborne noise caused by the radial vibration of the rotor back iron and the tangential vibration of the stator poles.

III. ACOUSTIC NOISE MODELING CONSIDERATIONS

A. MECHANISM OF VIBRATION GENERATION

As shown in Fig. 2, both the radial and tangential components of the electromagnetic force can cause vibrations in different ways. The radial forces can excite the radial vibration modes and cause radial vibration in the back iron. On the other hand, tangential vibration modes of the poles can be excited by the tangential forces, which generates tangential vibration in the poles.

Both the radial vibration modes of the stator and rotor can be excited by the radial forces and, thus, cause vibration and acoustic noise. For an IR SRM, the radial stiffness of the stator back iron is typically smaller than that of the rotor. However, the reverse is usually true for ER SRMs due to smaller rotor back iron thickness and larger rotor diameter in ER SRMs.

As an example, Fig. 3 shows two different radial vibration modes of the rotor and stator in a 24/16 IR SRM. The natural frequency of the mode three of the rotor (11504 Hz) is much higher than that of the stator (3112 Hz) for the 24/16 IR SRM. Similarly, the natural frequency of the rotor mode two is also higher than that of the stator. Because the natural frequencies of the rotor radial vibration modes in an IR SRM are much higher, they are typically more difficult to excite compared to those of the IR SRM stator. A similar case usually applies to the ER SRM stator. Due to much higher natural frequencies of the stator radial vibration modes in ER SRMs, they are more difficult to excite compared with the rotor radial vibration modes of the ER SRM. As an example, the difference in the

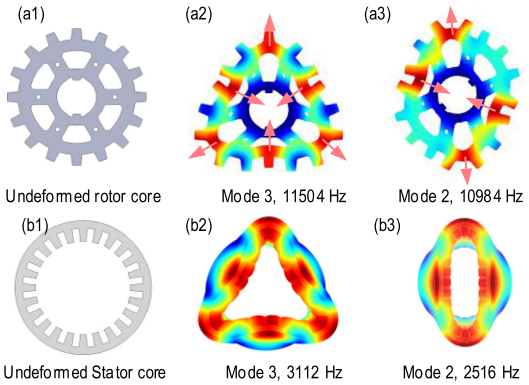

FIGURE 3. Radial vibration modes of the yokes in a 24/16 IR SRM, (a) rotor, (b) stator.

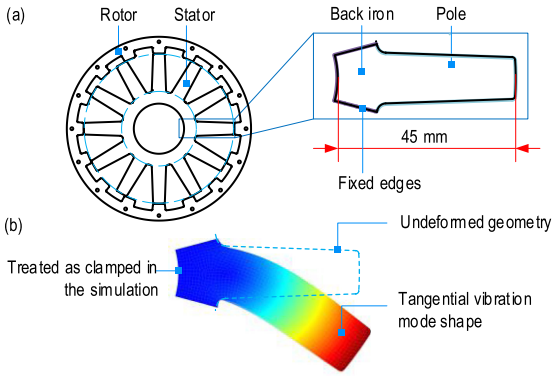

FIGURE 4. 12/16 ER SRM stator pole tangential vibration mode, modeled as a cantilever; (a) geometry, (b) first tangential vibration mode shape.

TABLE I. The Natural Frequencies of the Radial Vibration Mode Two and the Tangential Vibration Mode one for Several SRMs

SRM configuration	6/4	6/14	24/16	8/6	12/16	18/24
SRM construction, IR or ER	IR	IR	IR	IR	ER	ER
Rotor outer diameter [mm]	90	98.4	183	89.3	220	279
Stator outer diameter [mm]	160	139.2	264	170	179.2	241
Rotor inner diameter [mm]	25	12.7	50	30	180	242
Stator inner diameter [mm]	90.6	99.2	184	90	60	167
Rotor stack length [mm]	75	74	92	90	39.5	27
Rotor pole height [mm]	15	7	14.5	10.2	8	8
Stator pole height [mm]	19.7	10	25	23	45	26
Stator radial vibration mode two, [Hz]	2112	1885	2516	1896	*	*
Rotor radial vibration mode two, [Hz]	*	20,985	10,984	*	2938	852
The tangential vibration mode one of a single stator pole, [Hz]	31,192	54,751	18,565	21,996	6,243	15,100
The tangential vibration mode one of a single rotor pole, [Hz]	39,329	83,236	38,575	44,603	65,155	82,857

*The vibration mode is not found within 100 kHz.

natural frequencies of the radial vibration mode two of the stator and rotor for several IR and ER SRMs are presented in Table I. The material properties for the modal simulation in the 8/6, 6/4, 6/14, 24/16 IR SRM, 18/24, 12/16 ER SRM are 0.285 for Poisson's ratio, 7.6 g/cm^3 for mass density, and 175 GPa for Young's modulus, which were calculated using the method provided in [16] and the properties of the winding and lamination steel material provided in [17] and [18], respectively. It should be noted that radial vibration mode two is not excited in all these SRM topologies. The radial vibration modes to be excited by the electromagnetic forces depend on the number of phases and the number of stator poles [6], [8], [15]. For the 12/16 ER SRM prototype, the radial vibration modes to be excited will be discussed in Section VI.

B. TANGENTIAL VIBRATION MODES

As shown in Fig. 4, a simulation was conducted to show that the long height of a single pole can significantly reduce the natural frequency of the tangential vibration mode of a stator or rotor pole. Table I compares the natural frequency of the tangential mode one for a single pole in several SRM configurations. It should be noted that the tangential vibration mode of a single pole would be different than the tangential vibration mode of the stator-shaft subassembly. For the modal simulation of the stator-shaft subassembly, the boundary condition is applied to the shaft. In the modal simulation of a single stator or a rotor pole, the boundary condition is applied to the inner surface of the back iron, which was treated as clamped as depicted in Fig. 4. The natural frequencies of the first tangential vibration mode of the stator and rotor poles in 8/6, 6/4, 24/16, 6/14 IR SRM are close to or exceed 20 kHz (the upper range of human hearing). For IR SRMs operating below 10,000 RPM, the forcing frequencies of the electromagnetic force harmonics are usually less than 10 kHz. Therefore, the tangential vibration modes of poles in IR SRMs are often difficult to excite.

In contrast, for the 12/16 ER SRM, the natural frequency of the first tangential vibration mode of the stator pole is 6243 Hz, which is due to the lower stiffness caused by the long stator pole height. This is well within the human hearing range and, thus, it is possible for the stator tangential vibration to contribute to the total acoustic noise in ER SRMs; particularly if resonance with the tangential vibration modes occurs. In the following sections, the acoustic noise caused by the radial vibration of the rotor and the tangential vibration of the stator will be compared.

C. ACOUSTIC MODELING CONSIDERATIONS

As shown in Fig. 5, two numerical models are built to study and compare the vibration behavior and the acoustic noise of the motor subassemblies: (a) rotor subassembly (see Fig. 6(b)) to simulate the radial vibration of the rotor, (b) stator subassembly (see Fig. 6(c)) to simulate the tangential vibration of the stator poles. In each numerical model, the vibration modes and nodal forces are calculated. The right side of Fig. 5 depicts the analysis of the radial and tangential force density harmonics, and the simulation of the vibration and acoustic

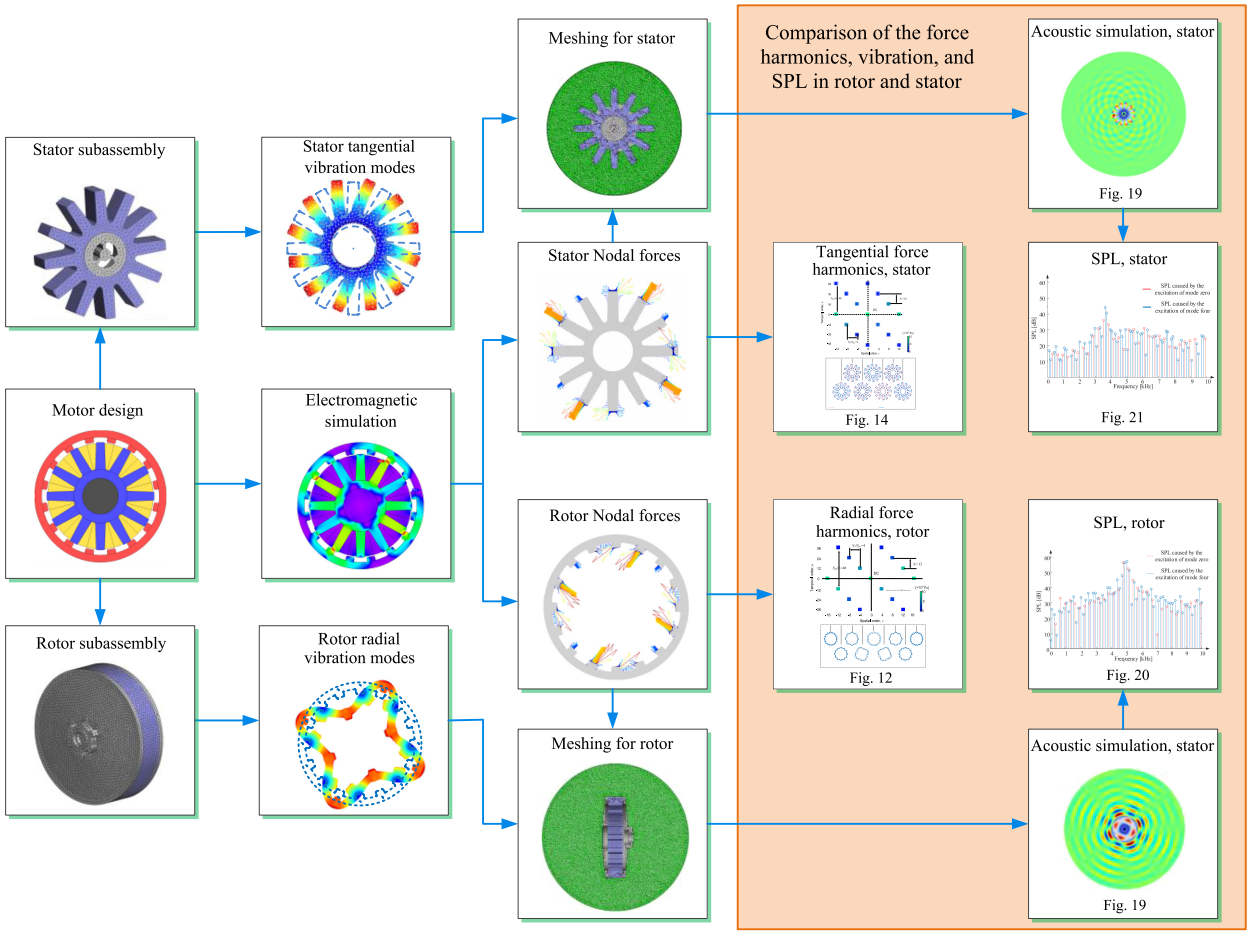

FIGURE 5. **Two acoustic noise models for the rotor and stator subassemblies.**

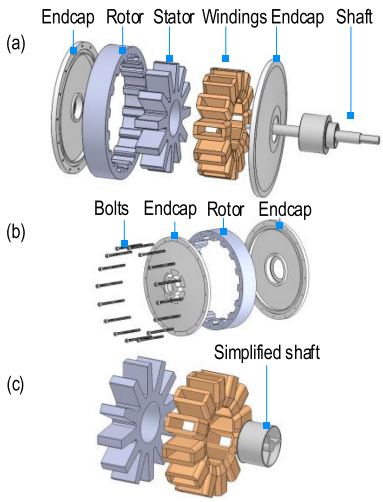

FIGURE 6. **Assembly of the 12/16 E-bike SRM, (a) motor assembly, (b) rotor-endcaps subassembly, (c) stator-shaft-winding subassembly.**

noise, which will be discussed in detail in the upcoming sections. The electromagnetic FEA simulation and the numerical simulation of vibration and acoustic noise were conducted in JMAG and Actran, respectively.

Fig. 6 shows the motor assembly, rotor-endcaps subassembly, and the stator-shaft subassembly of the 12/16 ER SRM. The geometry of the shaft is simplified to reduce the required thickness in the meshing of the near field (to reduce the computation cost) without sacrificing the accuracy). It should be noted that the contact between the rotor and the endcaps affects the simulation accuracy. Fig. 7 shows how the contacts between the rotor and the endcaps are built. In the prototype of this motor, the rotor and the endcaps are connected using fasteners (e.g. bolts). In order to model the contact between the rotor and the endcaps correctly, only the nodes at the bolt area of the rotor-endcap interface should be merged, as shown in Fig. 7(b). The boundary conditions for the simulation of the natural frequencies in the stator-shaft subassembly and the rotor-endcaps subassembly are shown in Fig. 8.

For the simulation of the acoustic noise, the meshing of the near field and the motor structures for the rotor-endcaps and stator-shaft subassemblies are shown in Fig. 9. The element size and radius of the near field meshing were calculated and carefully selected to ensure simulation accuracy. The calculation of the required element size and radius of the near-field meshing is presented in [7], [8].

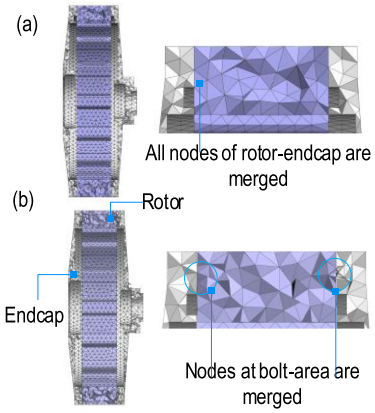

FIGURE 7. Contacts between parts in the modal simulation for the rotor subassembly [8].

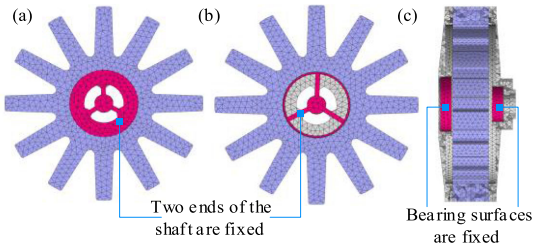

FIGURE 8. Boundary conditions, (a) front view of the stator-shaft subassembly, (b) back view of the stator-shaft subassembly, (c) rotor-endcaps subassembly.

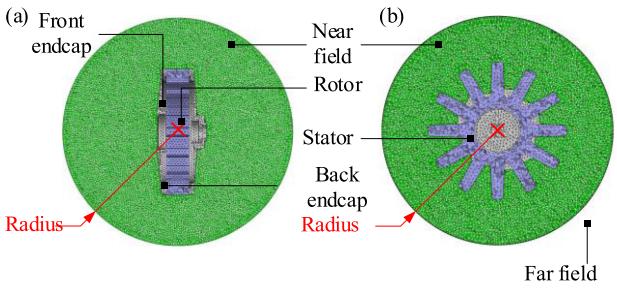

FIGURE 9. Meshing of the motor structure and the near field, (a) rotor-endcaps subassembly, (b) stator-shaft subassembly.

IV. ROTOR RADIAL VIBRATION MODES AND RADIAL FORCE DENSITY ANALYSIS

A. ROTOR RADIAL VIBRATION MODES

The numerical simulation of the vibration modes of the stator and the rotor is conducted in ACTRAN. The details of the numerical modeling are presented in [7], [8]. Fig. 10 shows the radial vibration modes of the rotor-endcaps subassembly, where the free deformation and vibration appear in the radial direction. It will be shown in Section IV.B that the radial vibration mode zero (M-R0) and mode four (M-R4) are the dominant vibration modes of the rotor-endcaps subassembly.

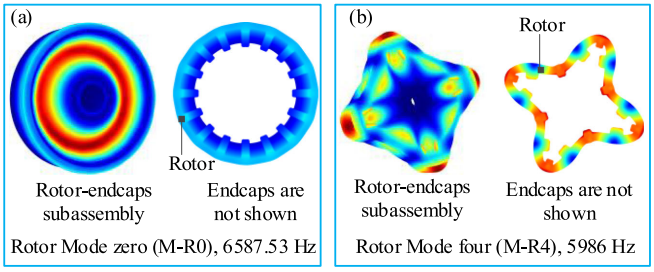

FIGURE 10. Dominant radial vibration modes of the rotor-endcaps subassembly, (a) Mode zero (M-R0), (b) Mode four (M-R4).

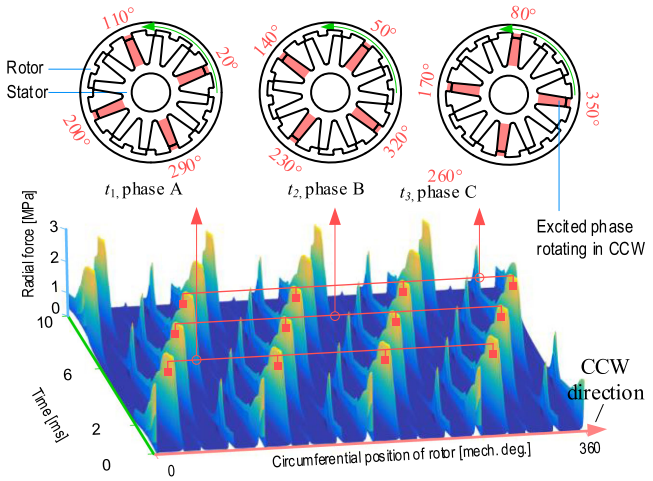

FIGURE 11. The radial force density waveform of the rotor in a 12/16 ER SRM at 400 rpm and with a reference phase current of 75 A [15].

B. ROTOR RADIAL FORCE DENSITY HARMONICS

As depicted in Fig. 5, the tangential force density of the stator pole tip and the radial force density of the rotor pole tip are extracted from a 2D electromagnetic FEA simulation. Before presenting the analysis and discussion of the simulated vibration and the acoustic noise of the 12/16 ER SRM, the harmonic components (including the magnitude, temporal, and circumferential order) of the stator tangential force density and the rotor radial force density need to be analyzed. The harmonics of the stator tangential force density and rotor radial force density are obtained by applying 2D FFT to the surface waveforms of the electromagnetic force density.

The surface wave of the rotor electromagnetic force was measured at different time steps and circumferential positions in the electromagnetic FEA simulation. The waveform of the rotor electromagnetic force is shown in Fig. 11. At t_1, Ph#A is excited and four force spikes appear at 20, 110, 200, 290 [mech. deg]. At t_2, Ph#B is excited and the four spikes of the radial force appear at 50, 140, 230, 320 [mech. deg]. Similarly, at t_3, Ph#C is excited and there are four spikes of the radial force appearing at 80, 170, 260, 350 [mech. deg]. After applying 2D FFT to the data of this electromagnetic force

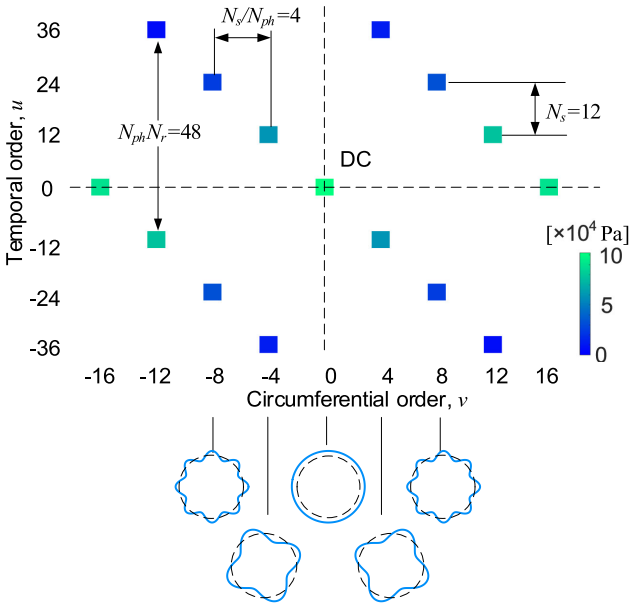

FIGURE 12. Radial force density harmonics of the 12/16 ER SRM rotor when the rotor rotates at 400 RPM, CCW direction, with a reference current of 75A, turn-on angle, $\theta_{on} = -77.9$ [elec. deg.], turn-off angle, $\theta_{off} = 114.1$ [elec. deg.].

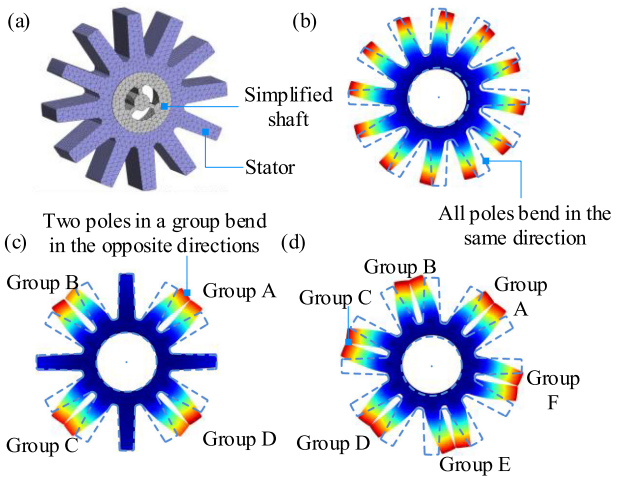

FIGURE 13. Dominant Vibration modes of the stator with 12 poles, (a) undeformed structure, (b) tangential mode zero (M-S0), 3988 Hz, (c) tangential mode four (M-S4), 4186 Hz, (d) tangential mode six (M-S6), 4137 Hz.

waveform, and the harmonic components can be obtained as shown Fig. 12.

The temporal order, u, and the motor speed, n (in RPM), can be used to calculate the forcing frequency of the force density harmonic, f, where $f = |u| \times n / 60$. The circumferential order, v, is related to the shape of the force density harmonic [19].

The radial force density harmonics of the rotor of the 12/16 ER SRM are shown in Fig. 12. When $|v| \leq 8$, the harmonics in the rotor radial force density excite the same circumferential order of the radial vibration mode. For example, the radial force harmonics with $|v| = 4$ excite the radial vibration mode four (M-R4).

V. STATOR TANGENTIAL VIBRATION MODES AND TANGENTIAL FORCE DENSITY ANALYSIS

A. TANGENTIAL VIBRATION MODES

For the tangential vibration modes of the stator poles, it is important to note that a pole can vibrate and bend in either the positive (counter clockwise) or negative (clockwise) direction. Fig. 13 shows the vibration modes of the stator of the ER SRM. In Fig. 13(b), the tangential vibration mode zero (M-S0) of the stator-shaft subassembly is shown. It can be seen that all the stator poles bend in the same direction. Tangential vibration mode zero (M-S0) is one of the dominant vibration modes for the stator-shaft subassembly. This will be verified in the analysis of the electromagnetic force density harmonics in Section V.B and the simulated sound pressure level (SPL) diagram in Section VI.C. Tangential mode four (M-S4) is shown in Fig. 13(c). It can be seen that there are four groups of stator poles with significant free deformation. Each group consists of two stator poles and these two poles bend in opposite directions.

Tangential mode six (M-S6) is shown in Fig. 13(d), where six groups of stator poles with significant free deformation can be observed. It can be concluded that the largest tangential vibration mode of the stator is limited by the number of stator poles. For this stator with twelve poles, mode six is the largest mode number of the tangential vibration mode. Any tangential vibration mode that has a mode number higher than six does not exist for this stator. This is not the case for the radial vibration modes of the rotor. The largest mode number of the radial vibration mode is not related to the number of rotor poles. This is because the rotor poles can be regarded as additional mass and stiffness attached to the rotor back iron.

B. TANGENTIAL FORCE DENSITY HARMONICS

Fig. 14 shows the tangential force density harmonics of the 12/16 ER SRM stator. Since the tangential force density is applied in the tangential direction, it only causes tangential vibration on the stator poles. Fig. 14 also shows how different tangential vibration modes of the stator will be excited. When $|v| \leq 4$, the tangential force density harmonics excite the corresponding circumferential order of the tangential vibration mode. When $|v| > 4$, the corresponding tangential vibration mode cannot be excited. This is related to the available tangential vibration modes and the tangential force density harmonics. In this 12-pole stator, mode six is the largest mode number of the tangential vibration modes, as shown in Fig. 13. As mentioned earlier, tangential vibration modes higher than six do not exist in 12/16 ER SRM. In terms of the tangential force density harmonics shown in Fig. 14, the 6th circumferential order ($|v| = 6$) does not exist, because 12/16 ER SRM is a four-pole motor and the circumferential orders, v are in multiples of four.

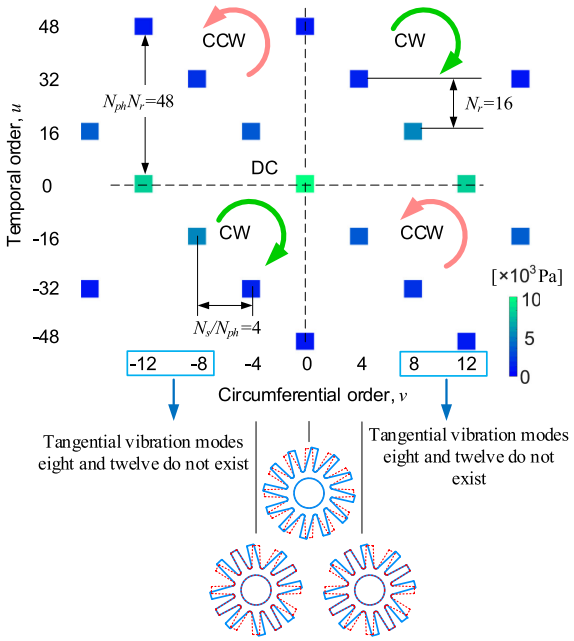

FIGURE 14. Tangential force density harmonics of the 12/16 ER SRM stator when the rotor rotates at 400 RPM, CCW direction, with a reference current of 75A, $\theta_{on} = -77.9$ [elec. deg.], $\theta_{off} = 114.1$ [elec. deg.].

VI. RESULTS AND DISCUSSIONS

A. PATTERN OF FORCE DENSITY HARMONICS IN THE STATOR AND ROTOR

The rotor radial force density harmonics and the stator tangential force density harmonics at 400 RPM were discussed and shown in Fig. 12 and Fig. 14. In this section, the pattern of the force density harmonics will be discussed. The temporal order, u and circumferential order, v of the rotor radial force density harmonics and the stator tangential force density harmonics can be summarized by using (1) and (2), respectively. The derivation of these expressions has been presented in [8] and [15]. It should be noted that these two equations are related to the topology, the phase excitation sequence, and the rotor rotational direction of the 12/16 external-rotor SRM. Equations (1) and (2) are used to analyze the frequency components of simulated and tested acoustic noise.

$$\text{For rotor} \begin{cases} u = N_r \times N_{ph} \times j - N_s \times k = 48 \times j - 12 \times k \\ v = \dfrac{N_s}{N_{ph}} \times k = 4 \times k \end{cases} \tag{1}$$

$$\text{For stator} \begin{cases} u = N_r \times N_{ph} \times j - N_r \times k = 48 \times j - 16 \times k \\ v = \dfrac{N_s}{N_{ph}} \times k = 4 \times k \end{cases} \tag{2}$$

where j and k can be any arbitrary integer, N_r is the number of rotor poles, N_s is the number of stator poles.

The harmonics with $|v| = 0$, 4, and 8 are shown in Table II. Please note that the temporal orders for the 0^{th}-circumferential-order harmonics of the rotor and the stator are the same. This is because in this case the temporal orders for the harmonics of the stator and the rotor are only related to the number of strokes, $N_r \times N_{ph}$. Table III shows the frequencies of the dominant harmonics when the motor operates at 400 RPM. These frequency points will be used in Sections VI. C and D to explain the simulated and tested SPL.

TABLE II Temporal and Circumferential Orders, ($|u|$, $|v|$) of the Harmonics in the Force Density of 12/16 ER SRM Rotor and Stator When the Rotor Rotates in the CCW Direction

Part	Force component	Temporal order, $\|u\|$	Circumferential order, $\|v\|$
Stator	Tangential	48, 96, 144, …|48 × j|	0
		16, 32, 64, …, |-16 + 48 × j|	4
		16, 32, 64, …, |-32 + 48 × j|	8
Rotor	Radial	48, 96, 144, …, |48 × j|	0
		12, 36, 60, , …, |-12 + 48 × j|	4
		24, 72, 120, …, |-24 + 48× j|	8

*j can be any integer.

TABLE III Frequencies of the Harmonics in the Force Density of 12/16 ER SRM Rotor and Stator When the Rotor Rotates at 400 RPM, CCW Direction

Part	Force component	Frequency [Hz]	Circumferential order, $\|v\|$
Stator	Tangential	320, 640, 960, …, |48 × j| × 6.67	0
		106.7, 213.3, 426.7, …, |-16 + 48 × j| × 6.67	4
Rotor	Radial	320, 640, 960, …, |48 × j| × 6.67	0
		80, 240, 400, …, |-24+48 × j| × 6.67	4

*j can be any integer.

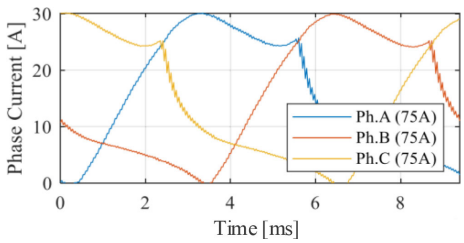

FIGURE 15. Current waveform used in the simulation and experimental test: at 400 RPM with a reference current of 75A, $\theta_{on} = -77.9$ [elec. deg.], $\theta_{off} = 114.1$ [elec. deg.] [13].

B. COMPARISONS OF SIMULATED VIBRATIONS

Following the modeling and simulation procedures presented in Fig. 5, the vibration behavior and the acoustic noise are simulated by using numerical methods. The current waveform used in the electromagnetic simulation and the experimental test is shown in Fig. 15. PWM current control with a switching frequency of 10 kHz is used. The turn-on and turn-off angle of the current waveform for the given speed and reference current, were optimized using multi-objective Genetic Algorithm (GA) optimization, which is based on the experimentally tested flux linkage and the measured phase resistance of the motor prototype. Then the current waveform

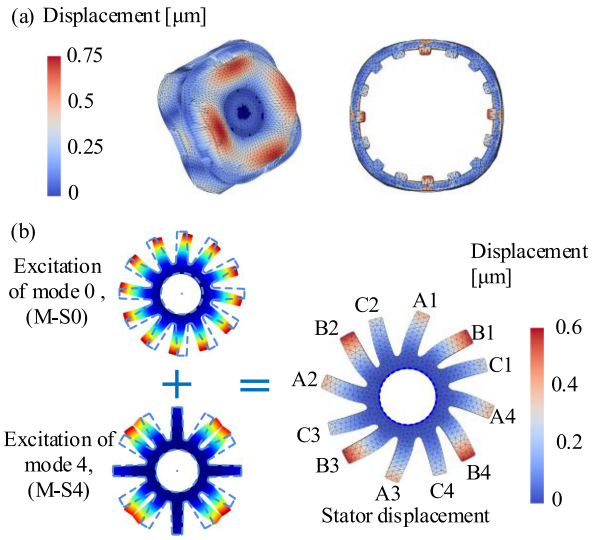

FIGURE 16. Simulated transient displacement at $t = 0.019$s in the 12/16 external-rotor SRM operating at 400 RPM with a reference current of 75 A, $\theta_{on} = -77.9$ [elec. deg.], $\theta_{off} = 114.1$ [elec. deg.], (a) rotor and endcaps, (b) stator.

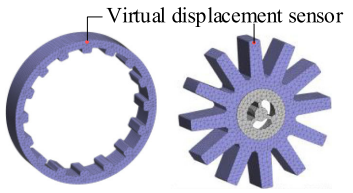

FIGURE 17. Locations of the virtual displacement sensors.

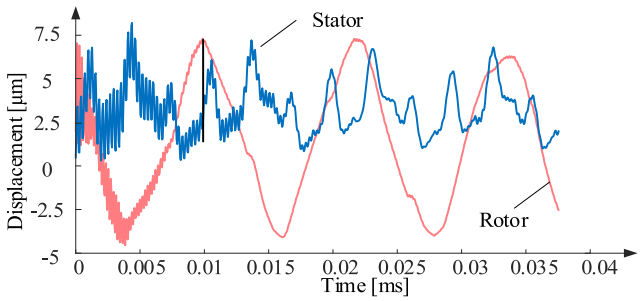

FIGURE 18. Tangential displacement of the stator and the radial displacement of the rotor in the 12/16 external-rotor SRM, at 400 RPM with a reference phase current of 75 A, $\theta_{on} = -77.9$ [elec. deg.], $\theta_{off} = 114.1$ [elec. deg.].

was obtained from a dynamic model, which also uses the experimental flux linkage. Fig. 16 shows the displacement of the rotor and the stator of the 12/16 ER SRM at 400 RPM with a reference current of 75 A at $t = 0.19$ s. It can be seen that the displacement of the rotor is a combination of the displacements caused by the excitations of the radial vibration mode four (M-R4) and zero (M-R0). The displacement of the stator, which is shown in Fig. 16(b), is caused mainly by the excitation of the tangential vibration mode zero (M-S0, see Fig. 13(b)) and four (M-S4, see Fig. 13(c)). In Fig. 16(b), all the stator poles bend in the clockwise direction, because for tangential vibration mode zero (M-S0), all the stator poles have the same displacement in the same direction as shown in Fig. 13(b). However, in Fig. 16(b), the stator poles of different phases have different displacements. Medium displacement can be observed on the stator poles A1, A2, A3, and A4. These stator poles belong to Phase A. The stator poles of Phase B (B1, B2, B3, and B4) have the largest displacement, and the stator poles of Phase C (C1, C2, C3, and C4) have the smallest displacement. This is due to vibration mode four (M-S4).

As shown in Fig. 13(c), for vibration mode four (M-S4), the stator poles vibrate in groups. Each group includes the stator poles of two different phases, which bend in opposite directions. The stator poles of the remaining phase do not have significant displacement. In Fig. 16(b), stator poles of Phase C and Phase B are the poles that belong to the vibrating groups of vibration mode four (M-S4). For vibration mode four (M-S4), the stator poles of Phase B bend in the same direction as in vibration mode 0 (M-S0). This is the reason why the stator poles B1, B2, B3, and B4 have the largest displacement. In vibration mode four (M-S4), the stator poles of Phase C bend in the opposite direction as compared to vibration mode 0 (M-S0). This is the reason why stator poles C1, C2, C3, and C4 have the lowest displacement. In Fig. 16(b), the stator poles of Phase A do not belong to the group that vibrates in vibration mode four. Therefore, in this vibration mode, they do not have significant displacement. This is the reason why the stator poles A1, A2, A3, and A4 have the medium displacement in Fig. 16(b).

In order to further compare the vibration behavior of the rotor and the stator, virtual displacement sensors are placed on the rotor and the stator (see Fig. 17). The captured displacements of the stator and the rotor are shown in Fig. 18. The noise at the beginning of the simulated displacement is the transient response of the mechanical vibration and decreases quickly to almost zero after $t = 0.018$s because of the damping and friction effect of the motor structure. It can be seen that the rotor has a higher vibration magnitude than the stator. The stator and rotor displacement waveforms have many harmonic components. All these harmonics are sources of acoustic noise. However, since they have different radiation ratios and different forcing frequencies, the maximum SPL is not necessarily caused by the harmonic with the largest amplitude.

C. COMPARISONS OF SIMULATED ACOUSTIC NOISE

Fig. 19 compares the sound pressure of the rotor and the stator at an instantaneous time step. As shown in Fig. 19(a), for the rotor, the positive air pressure region designated by dashed lines is surrounded by two positive air pressure regions and two negative air pressure regions. This means that the sound pressure generated by the rotor travels in the radial direction only. The positive pressure regions can be considered as the peaks of a sinusoidal wave and the negative pressure regions as the troughs.

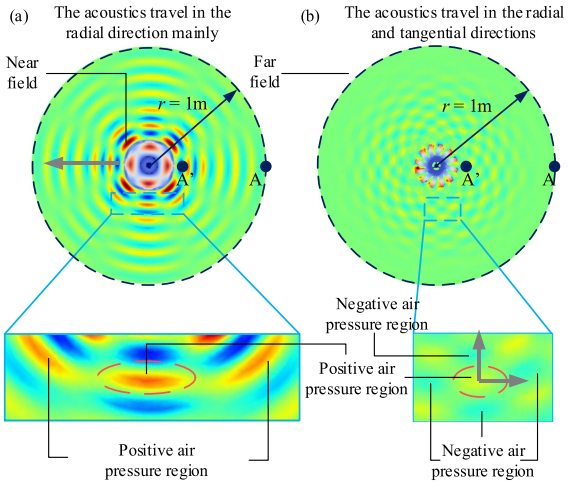

FIGURE 19. Comparison between the sound pressure caused by the vibration of the stator and the rotor, (a) rotor, (b) stator.

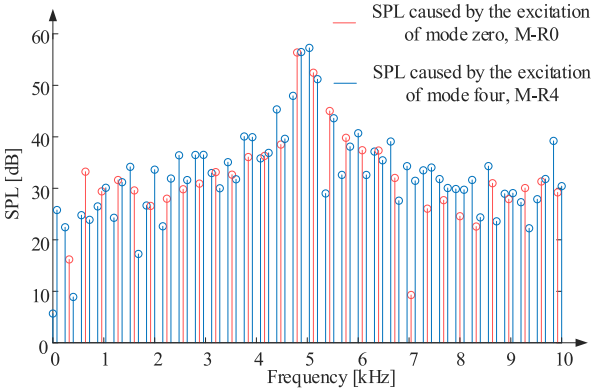

FIGURE 20. Sound pressure level radiated from the rotor of the 12/16 external-rotor SRM, 400 RPM with a reference current of 75 A, $\theta_{on} = -77.9$ [elec. deg.], $\theta_{off} = 114.1$ [elec. deg.].

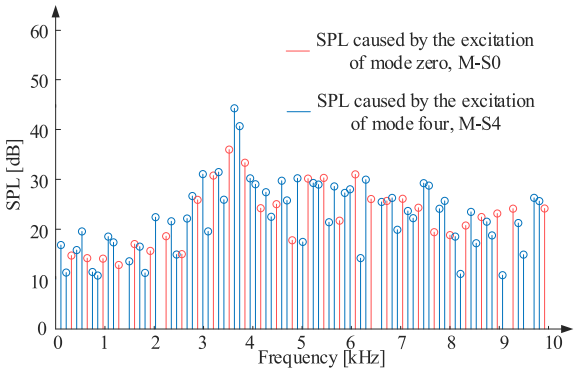

FIGURE 21. Sound pressure level radiated from the stator of the 12/16 external-rotor SRM, 400 RPM with a reference phase current of 75 A, $\theta_{on} = -77.9$ [elec. deg.], $\theta_{off} = 114.1$ [elec. deg.].

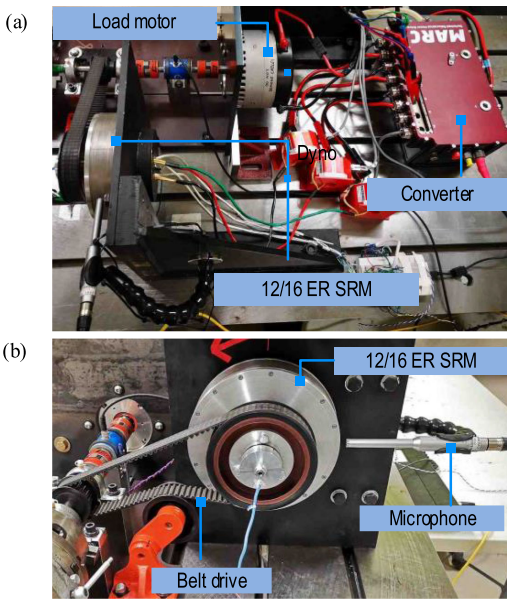

FIGURE 22. Setup for the acoustic noise measurement of 12/16 ER SRM, (a) top view, (b) front view.

In Fig. 19(b), for the stator, the positive pressure region designated by the dashed lines is surrounded by four negative air pressure regions. Therefore, the sound pressure caused by the stator travels in both the radial and the tangential directions. It travels in the tangential direction due to the tangential vibration caused by the stator poles as shown in Fig. 19(b). The sound pressure from the stator also travels in the radial direction. This is because the acoustic noise waveform needs to travel to the far field through the radial direction. In Fig. 19, A and A' are the two acoustic noise observation points located in the near field and the far field, respectively. It can be observed that the stator acoustic noise decreases at a faster rate than the rotor acoustic noise when the airborne noise travels from the near field to the far field.

Fig. 20 and Fig. 21 show the simulated SPL of the rotor and the stator of the 12/16 ER SRM at 400 RPM with a reference current of 75 A. The excitation of the stator tangential vibration mode zero (M-S0) and four (M-S4), and the rotor radial vibration mode zero (M-R0) and four (M-R4) cause the acoustic noise in this 12/16 ER SRM. The maximum SPL radiated from the rotor-endcaps subassembly is higher than the max SPL radiated from stator-shaft subassembly. It can be concluded that for the 12/16 ER E-bike SRM, which is designed with a thin rotor back iron and long stator poles, the acoustic noise caused by the radial vibration of the rotor dominates the total acoustic noise of the motor.

D. EXPERIMENTAL VALIDATIONS

The experimental setup for acoustic noise validation of the 12/16 ER SRM is shown in Fig. 22. The locations for the microphone in the experimental test and the virtual microphone in the acoustic noise simulation are identical, which is 20 cm away from the motor outer surface. During the acoustic measurement, thick blankets, which are not shown in Fig. 22, are used to cover the load motor in order to minimize its effect on the measured acoustic noise. Fig. 23 shows the tested

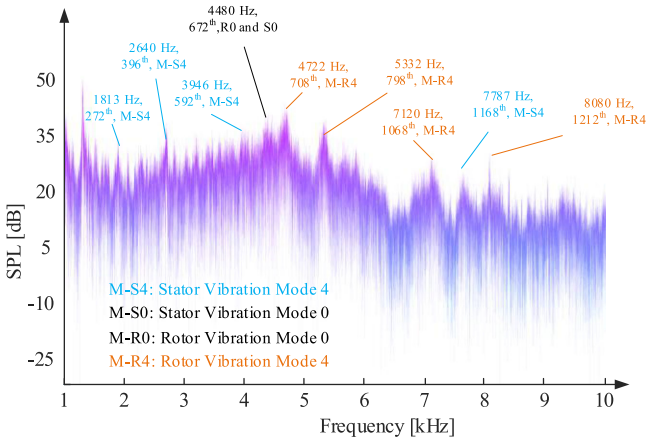

FIGURE 23. Experimental results of the SPL in the 12/16 external-rotor SRM, 400 RPM, with a reference phase current of 75 A, $\theta_{on} = -77.9$ [elec. deg.], $\theta_{off} = 114.1$ [elec. deg.].

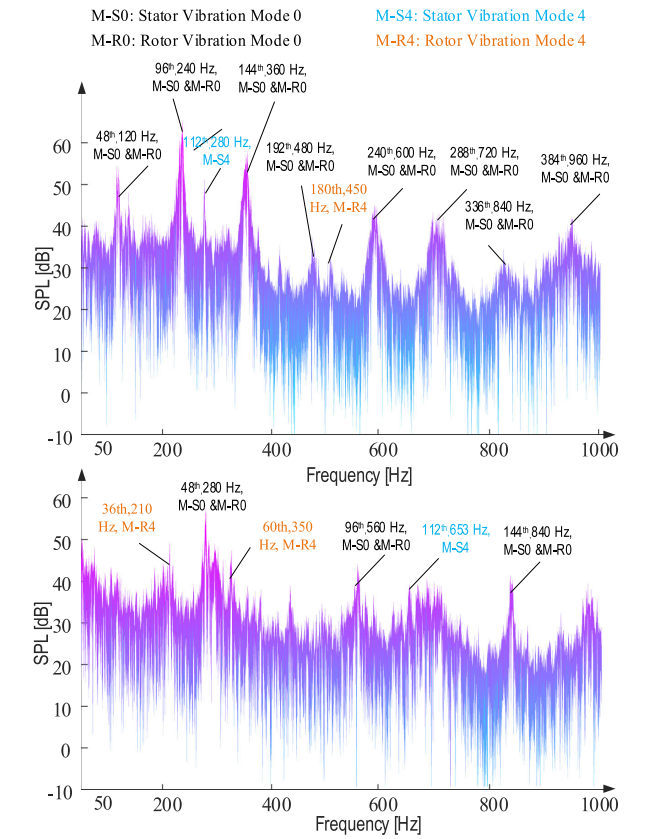

FIGURE 24. The tested SPL in the 12/16 ER SRM prototype with a reference current of 75 A, (a) at 150 rpm, (b) at 350 rpm.

SPL of the 12/16 ER SRM at 400 RPM and with a reference current of 75 A. The frequency, temporal order, and the source of the acoustic noise in each SPL peak are shown Fig. 23. The temporal order of the SPL peak can be calculated by the frequency of the SPL divided by the motor mechanical frequency. The source of the acoustic noise in each SPL peak can be identified by comparing the temporal order of the SPL and the temporal orders of the force density harmonics (see Table II). Many peaks of the SPL, which are caused by the numerous harmonics in the stator tangential force density and the rotor radial force density, can be observed in Fig. 23. Please note that some SPL peaks are caused by the simultaneous excitations of the rotor radial vibration mode zero (M-R0) and the stator tangential vibration mode zero (M-S0). The two SPL peaks that appear at 1280 Hz and 4480 Hz are such examples. As discussed in Section VI.A, this is because the temporal orders for the 0^{th} -circumferential-order harmonics in the stator tangential force density and the rotor radial force density are identical (see Table II), which are only related to the number of strokes, $N_r \times N_{ph}$.

Fig. 24 shows the tested SPL of the 12/16 ER SRM prototype with a peak reference current of 75A at 150 rpm and 350 rpm. The mechanical frequencies at 150 rpm and 350 rpm are 2.5 Hz and 5.83 Hz, respectively. The forcing frequencies of the rotor radial force density harmonics and the stator tangential force density harmonics at 150 rpm and 350 rpm can be calculated using the mechanical frequency and the temporal orders presented in Table II. It can be observed from Fig. 24 that both the radial vibration of the rotor back iron and the tangential vibration of the stator poles can be sources of the acoustic noise in this 12/16 ER SRM prototype.

V. CONCLUSION

In this paper, the rotor radial vibration and the stator tangential vibrations in an external rotor SRM have been presented. The harmonic components of the electromagnetic force density, the vibration modes, the vibration behavior, and the acoustic noise of the stator and the rotor are compared. A 12/16 external-rotor SRM designed for a direct-drive E-bike application is used in this paper for the modeling and analysis of vibration and acoustic noise. Results show that both the rotor radial vibration and the stator tangential vibration can be sources of acoustic noise in ER SRMs. For the 12/16 ER E-bike traction SRM, the acoustic noise caused by the radial vibration of the rotor back iron is larger than that caused by the tangential vibration of the stator poles. The modeling approach presented in this paper can also be used to identify the source of the acoustic noise for other ER-SRMs with different mass/stiffness properties.

ACKNOWLEDGMENT

The authors gratefully acknowledge Free Field Technologies (FFT), Powersys Solutions, CMC Microsystems and ANSYS for their support with ACTRAN software, JMAG software, Solidworks and ANSYS Workbench in this research, respectively.

REFERENCES

[1] S. Zuo, F. Lin, and X. Wu, "Noise analysis, calculation, and reduction of external rotor permanent-magnet synchronous motor," *IEEE Trans. Ind. Electron.*, vol. 62, no. 10, pp. 6204–6212, Oct. 2015.

[2] F. Lin, S. Zuo, W. Deng, and S. Wu, "Modeling and analysis of acoustic noise in external rotor in-wheel motor considering Doppler effect," *IEEE Trans. Ind. Electron.*, vol. 65, no. 6, pp. 4524–4533, Jun. 2018.

[3] W. Deng and S. Zuo, "Comparative study of sideband electromagnetic force in internal and external rotor PMSMs with SVPWM technique," *IEEE Trans. Ind. Electron.*, vol. 66, no. 2, pp. 956–966, Feb. 2019.

[4] J. Krotsch and B. Piepenbreier, "Radial forces in external rotor permanent magnet synchronous motors with non-overlapping windings," *IEEE Trans. Ind. Electron.*, vol. 59, no. 5, pp. 2267–2276, May 2012.

[5] S. M. Castano, B. Bilgin, J. Lin, and A. Emadi, "Radial forces and vibration analysis in an external-rotor switched reluctance machine," *IET Electric Power Appl.*, vol. 11, no. 2, pp. 252–259, Feb. 2017.

[6] J. Dong *et al.*, "Hybrid acoustic noise analysis approach of conventional and mutually coupled switched reluctance motors," *IEEE Trans. Energy Convers.*, vol. 32, no. 3, pp. 1042–1051, Sep. 2017.

[7] J. Liang *et al.*, "Prediction of noise and vibration of a 24/16 traction SRM," *IET Elect. Syst. Transp.*, vol. 10, no. 1, pp. 35–43, Mar. 2020.

[8] J. Jiang, J. Liang, J. Dong, B. Howey, and A. D. Callegaro, "Chapter 13: Noise and vibration in switched reluctance machines," *Switched Reluctance Motor Drives: Fundamentals to Applications*, Boca Raton, FL, USA: CRC Press, ISBN: 9781138304598, Nov. 2018.

[9] B. Bilgin *et al.*, "Modeling and analysis of electric motors: State-of-the-art review," *IEEE Trans. Transp. Electrific.*, vol. 5, no. 3, pp. 602–617, Sep. 2019.

[10] A. D. Callegaro, J. Liang, J. Jiang, B. Bilgin, and A. Emadi, "Radial force density analysis of switched reluctance machines: The source of acoustic noise," *IEEE Trans. Transp. Electrif.*, vol. 5, no. 1, pp. 93–106, Mar. 2019.

[11] B. Howey, E. Rowan, B. Bilgin, and A. Emadi, "Thermal trade-off analysis of an exterior rotor E-bike switched reluctance motor," in *Proc. IEEE Transp. Electrific. Conf. Expo.*, Chicago, IL, USA, 2017, pp. 605–612.

[12] B. Howey, "Non-coupled and mutually coupled switched reluctance machines for an E-bike traction application: Pole configurations, design, and comparison," Ph.D. thesis, Dept. Mech. Eng., McMaster Univ., Hamilton, Canada, 2018.

[13] B. Howey, B. Bilgin, and A. Emadi, "Design of an external-rotor direct-drive E-bike switched reluctance motor," *IEEE Trans. Veh. Technol.*, vol. 69, no. 3, pp. 2552–2562, Mar. 2020.

[14] Y. Yang, J. Jiang, and J. Liang, "Chapter 8: Mechanical construction of switched reluctance machines," *Switched Reluctance Motor Drives: Fundamentals to Applications*, Boca Raton, FL, USA: CRC Press, ISBN: 9781138304598, Nov. 2018.

[15] J. Liang, "Acoustic noise and vibrations in switched reluctance motors: enhanced modeling," Ph.D. thesis, Dept. Mech. Eng., McMaster Univ., Hamilton, Canada, 2019.

[16] R. Pupadubsin, A. Steven, J. D. Widmer, and B. C. Mecrow, "Mechanical material properties for structural simulation model of switched reluctance machines," in *Proc. IEEE Int. Conf. Elect. Mach.*, Lausanne, Switzerland, Sep. 2016, pp. 2293–2299.

[17] M. Bösing, "Acoustic modelling of electrical drives," Ph.D. thesis, RWTH Aachen Univ., Aachen, Germany, 2013.

[18] Cogent Power Inc., Typical data for SURA M470-50A. 2020. [Online]. Available: https://cogent-power.com/cms-data/downloads/m470-50a.pdf. Accessed: May 24, 2020.

[19] J. Jiang and J. Liang, "Chapter 12: Fundamentals of waves and vibrations," *Switched Reluctance Motor Drives: Fundamentals to Applications*, Boca Raton, FL, USA: CRC Press, ISBN: 9781138304598, Nov. 2018.

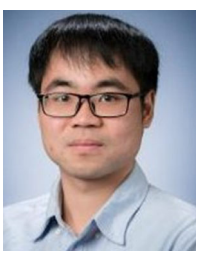

JIANBIN LIANG received the B.S. degree in mechanical engineering and the M.S. degree in vehicle engineering from Chongqing University, China, in 2012 and 2015, respectively, and the Ph.D. degree in mechanical engineering from McMaster University, Hamilton, ON, Canada in 2019. He is currently a Principal Engineer of Enedym, Inc., Hamilton, ON, Canada. His research interests include acoustic noise and vibration analysis, modeling and reduction, and the design of electric machines.

BROCK HOWEY (Member, IEEE) received the Ph.D. degree in mechanical engineering and the B.Tech degree in automotive and vehicle technology from McMaster University (Hamilton, Canada) in 2018 and 2014 respectively. From 2018–2019, he was a Postdoctoral Fellow at the Canada Excellence Research Chair (CERC) in hybrid powertrain program, at the McMaster Automotive Resource Center (MARC), where his research was directed toward switched reluctance and interior permanent magnet motor design. Dr. Howey is now the Principal Engineer at Enedym Inc., where he specializes in electric machine design.

BERKER BILGIN (Senior Member, IEEE) received the Ph.D. degree in electrical engineering from the Illinois Institute of Technology, Chicago, IL, USA, in 2011, and the MBA degree from the DeGroote School of Business, McMaster University, Hamilton, ON, Canada, in 2018. Dr. Bilgin is an Assistant Professor with the Department of Electrical and Computer Engineering (ECE), McMaster University. He is the Co-Founder and the Vice President of Engineering of Enedym Inc., Hamilton, ON, Canada, which is a spin-off company of McMaster University. Enedym specializes in electric machines, electric motor drives (EMDs), advanced controls and software, and virtual engineering. Dr. Bilgin has authored and co-authored 93 journals and conference papers and three book chapters. He is the Principal Inventor/Co-Inventor of ten patents and pending patent applications. His current research interests include electric machines, switched reluctance motor (SRM) drives, acoustic noise and vibration analysis and reduction, and power electronics and EMDs. He is the lead Editor and Author of the textbook titled *SRM Drives: Fundamentals to Applications*. Dr. Bilgin was the Elected General Chair of the 2016 IEEE Transportation Electrification Conference and Expo (ITEC). He also serves as an Associate Editor for the IEEE TRANSACTIONS ON TRANSPORTATION ELECTRIFICATION.

ALI EMADI (Fellow, IEEE) received the B.S. and M.S. degrees in electrical engineering with highest distinction from the Sharif University of Technology, Tehran, Iran, in 1995 and 1997, respectively, and the Ph.D. degree in electrical engineering from Texas A&M University, College Station, TX, USA, in 2000. He is the Canada Excellence Research Chair Laureate at McMaster University in Hamilton, Ontario, Canada. He is also the holder of the NSERC/FCA Industrial Research Chair in Electrified Powertrains and Tier I Canada Research Chair in Transportation Electrification and Smart Mobility. Before joining McMaster University, Dr. Emadi was the Harris Perlstein Endowed Chair Professor of Engineering and Director of the Electric Power and Power Electronics Center and Grainger Laboratories at Illinois Institute of Technology in Chicago, where he established research and teaching facilities as well as courses in power electronics, motor drives, and vehicular power systems. He was the Founder, Chairman, and President of Hybrid Electric Vehicle Technologies, Inc. (HEVT) – a university spin-off company of Illinois Tech. Currently, he is the President and Chief Executive Officer of Enedym Inc. and Menlolab Inc.—two McMaster University spin-off companies. He is the principal author/coauthor of over 500 journal and conference papers as well as several books including *Vehicular Electric Power Systems* (2003), *Energy Efficient Electric Motors (2004), Uninterruptible Power Supplies and Active Filters (2004), Modern Electric, Hybrid Electric, and Fuel Cell Vehicles (2nd ed, 2009), and Integrated Power Electronic Converters and Digital Control* (2009). He is also the editor of the *Handbook of Automotive Power Electronics and Motor Drives* (2005) and *Advanced Electric Drive Vehicles* (2014). He is the Co-Editor of the *Switched Reluctance Motor Drives* (2018). Dr. Emadi was the Inaugural General Chair of the 2012 IEEE Transportation Electrification Conference and Expo (ITEC) and has chaired several IEEE and SAE conferences in the areas of vehicle power and propulsion. He was the founding Editor-in-Chief of the IEEE TRANSACTIONS ON TRANSPORTATION ELECTRIFICATION from 2014 to 2020.